



## A transport-velocity formulation for smoothed particle hydrodynamics



S. Adami <sup>\*</sup>, X.Y. Hu, N.A. Adams

Institute of Aerodynamics, Technische Universität München, 85748 Garching, Germany

### ARTICLE INFO

#### Article history:

Received 27 September 2012

Received in revised form 30 January 2013

Accepted 31 January 2013

Available online 14 February 2013

#### Keywords:

Weakly-compressible SPH

Background pressure

Internal flows

### ABSTRACT

The standard weakly-compressible SPH method suffers from **particle clumping** and void regions for high Reynolds number flows and when negative pressures occur in the flow. As a **remedy**, a new algorithm is proposed that combines the homogenization of the particle configuration by a background pressure while at the same time reduces artificial numerical dissipation. The transport or **advection velocity** of particles is modified and an **effective stress term** occurs in the momentum balance that accounts for the difference between advection velocity **times** particle density and actual particle momentum. The present formulation can be applied for internal flows where the density summation is applicable. A wide range of test cases demonstrates unprecedented accuracy and stability of the proposed modification even at previously **infeasible** conditions.

© 2013 Elsevier Inc. All rights reserved.

### 1. Introduction

Smoothed particle hydrodynamics (SPH) is a fully Lagrangian, mesh-free method that was proposed 1977 independently by Lucy [1] and Gingold and Monaghan [2]. Originally, SPH was used to simulate astrophysical problems as its meshless nature and the exact advection are very attractive for these kind of problems. The key idea of SPH is to use a smoothing kernel to approximate field quantities at arbitrarily distributed discretization points (particles) and move these points with their local velocity. As a result of this smoothing technique, spatial derivatives are calculated only from interactions with any neighboring particles. In practice, the smoothing kernel has compact support to limit the number of interacting particles and the width of this kernel represents the discretization length scale of SPH.

In the past, SPH has been applied successfully to a broad range of problems beyond its original purpose. Different equations of motion can easily be incorporated by modifying the interactions between different particles, thus almost any continuum system that can be formulated in terms of partial differential equations can be discretized by SPH. A comprehensive overview of the capabilities of SPH is presented in the review article of Monaghan [3], where the principles of the method to simulate compressible flows (astrophysical problems) and incompressible fluid dynamics as well as solid mechanics within a unified framework are described.

Compared to mesh-based methods the evolution of a system in a Lagrangian framework offers many important advantages. Most obviously, advection is treated exactly by a Lagrangian particle method and exact conservation of mass and momentum is ensured in a straightforward way. Furthermore, for multi-phase problems the interaction-based force calculation allows for a modeling of very complex physical phenomena at phase interfaces without the need of additional surface-front detection algorithms. Large deformations and complex geometry changes such as fragmentation can be treated implicitly with SPH and the required **preprocessing** of a simulation is small.

\* Corresponding author. Tel.: +49 89 28916122.

E-mail address: [stefan.adami@tum.de](mailto:stefan.adami@tum.de) (S. Adami).

When solving incompressible fluid dynamics with SPH there are mainly two basic strategies, namely a true incompressible formulation (ISPH) and the weakly compressible model (WCSPH). In the former method a pressure Poisson equation is solved and the divergence condition for the velocity field is enforced, see e.g. [4–6]. This approach was shown to give accurate results for free-surface and multiphase flows but the computational complexity is high. The latter approach treats the fluid as weakly compressible with an equation of state that relates the fluid density to a hydrodynamic pressure. Given that the magnitude of the speed of sound and the characteristic flow velocities are well separated, density fluctuations remain small and the fluid behaves quasi-incompressible. Due to its simplicity and lower computational cost this method is widely used for various kinds of problems, see e.g. [7–11].

In this work we propose a new transport-velocity formulation for weakly-compressible SPH that resolves an important **dilemma** of the classical WCSPH scheme. According to the theory of incompressible flow, the pressure in the fluid takes effect merely by its gradient. Therefore, the flow is invariant of a **superimposed** constant background pressure field, i.e. it is gauge invariant. However, since the standard SPH is not 0th-order consistent, gauge invariance is not recovered numerically, leading to a **spurious** pressure gradient from a formally constant pressure field. Hence, the simulation results change with different background pressures. Ideally, no background pressure should need to be added to the system. On the other hand, when a low (zero) background pressure is imposed, SPH suffers from the so-called tensile instability. This instability is caused by particle clumping due to attraction forces between neighboring particles with effectively negative pressures. A possible solution to this problem is to increase the background pressure that ensures non-negative pressures in the entire domain, but as mentioned before this introduces additional numerical viscous dissipation that can be comparable to the physical viscous dissipation. Thus, increasing the background pressure effectively changes the Reynolds number of the flow, and consequently the application of SPH to practical industrial applications is substantially **impeded**. Note that our method mainly addresses the tensile instability problem, a “cousin of the pairing instability” with the same **symptoms** [12]. As a **side-effect** we found that with the new method the pairing instability [13] does not occur either. Alternatively the latter instability could also be circumvented by using kernels that have non-negative kernel Fourier transforms [12,14].

In 1989 Monaghan [15] addressed the problem of penetration in particle methods and proposed a modified advection velocity based on a smoothing of the velocity field. This so-called XSPH correction can improve the smoothness of the flow field, but, strictly speaking, the smoothing is arbitrary involving an unknown parameter. Another classical **workaround** for the clumping problem is to use an artificial viscosity that stops particles approaching each other when they are very close, e.g. Monaghan [3]. Whilst this artificial dissipation can be shown to take effect as a physical viscosity, and thus is used to simulate real flows at finite Reynolds numbers, at the same time the numerical dissipation required to stabilize the simulation of high Reynolds number flows can become comparable to the physical viscosity and of course strongly affects the results.

For truly incompressible SPH methods the particle clumping problem is easily suppressed as the divergence-free condition for the velocity field and the constant-density condition can be enforced separately. Hu and Adams [4] use a fractional time-step integration with an intermediate projection step and experienced no problems with particle penetration. Xu et al. [6] proposed an ISPH method that takes advantage of an additional diffusion-based particle shifting scheme ensuring well homogenized particle configurations at all times. Very recently, Lind et al. [16] extended this approach for free-surface problems where the standard method failed due to the incomplete kernel support of particles at the free surface. Additionally, they use the kernel gradient normalization and approximate the shifted particle quantities by a Taylor series to improve the accuracy of the scheme.

As a new, fundamentally different approach, we present here a simple and effective algorithm based on the classical WCSPH without need for additional parameters and involving only a marginally small computational overhead. The new method is characterized by the different utilization of a background pressure on computing the particle momentum velocity and the particle advection velocity. As a consequence of the new advection velocity, an additional term appears in the momentum equation that accounts for the difference between the motion of a particle and its averaged momentum. In more detail, the particle advection velocity is obtained from the momentum velocity corrected for the effect of a constant background pressure. Thus, regularization of the particle motion is achieved by the background pressure but the particle momentum is unaffected, i.e. no artificial dissipation of momentum occurs. The correction term in the momentum equation due to the different velocities acts as an effective stress and can be discretized in conservative form. While this correction is negligible when the flow is well resolved with the given size of a particle, it has considerable effects when the flow is not well resolved, e.g. for huge Reynolds numbers, and helps to prevent particle clustering. We point out that the present method is currently limited to internal flows. Free surfaces and inner surfaces of breaking waves for example would be treated as empty space and be filled with particles. An extension of this method for such cases requires the incorporation of suitable boundary conditions at the free surface and is subject of current work.

After describing our new method in detail in Section 2 we present many classical test problems of SPH in Section 3. The results show that our scheme prevents voids and particle clustering while strongly reducing numerical dissipation compared to standard WCSPH. Allowing for stable simulations at high Reynolds numbers, this method strongly extends the capabilities of SPH to simulate real applications. Finally, concluding remarks are given in Section 4.

## 2. Method

In this section we present our method in detail and focus on the new particle transport or advection velocity. We initialize all our simulations with Cartesian particles using a constant particle spacing  $\Delta x$ . Each particle is assigned a constant mass and the density is calculated using the density summation at every time step. Thus, mass conservation is satisfied exactly. We solve the incompressible Navier–Stokes equations in a Lagrangian frame and consider external body forces, viscous forces and pressure forces. Note, our general formulation holds for multi-phase problems as well (see the Rayleigh–Taylor instability in Section 3.6), but in the current work we do not include surface-tension effects. Fluids are treated as weakly compressible using an equation-of-state to relate the pressure to the density, and viscous effects are incorporated with a physical viscosity model [8] rather than an artificial viscosity.

In XSPH [15] particles are moved with a smoothed velocity field to prevent particle penetration. Here, we do not advect particles with the momentum velocity but use an advection velocity  $\tilde{\mathbf{v}}$  which is defined as the momentum velocity corrected by a pressure force due to an arbitrary but constant pressure field. Effectively, this advection velocity maintains a homogeneous particle distribution while it avoids the classical background-pressure problem in the momentum equation. Introducing the modified advection velocity into the conservation law for the momentum of a Lagrangian particle, for clarity using index notation, we obtain

$$\frac{\partial(\rho v_i)}{\partial t} + \tilde{v}_j \frac{\partial(\rho v_i)}{\partial x_j} - \tilde{v}_j \frac{\partial(\rho v_i)}{\partial x_j} + v_j \frac{\partial(\rho v_i)}{\partial x_j} = [\dots]_i - \rho v_i \frac{\partial v_j}{\partial x_j}, \quad (1)$$

where  $[\dots]_i$  is short for the other components of the right-hand-side (pressure force, viscous force and body force). Defining the material derivative of a particle moving with the modified advection velocity  $\tilde{\mathbf{v}}$  as

$$\frac{\tilde{d}(\bullet)}{dt} = \frac{\partial(\bullet)}{\partial t} + \tilde{\mathbf{v}} \cdot \nabla(\bullet) \quad (2)$$

we rearrange the momentum equation to obtain

$$\frac{\tilde{d}(\rho v_i)}{dt} = [\dots]_i + \frac{\partial}{\partial x_j} (\rho v_i (\tilde{v}_j - v_j)) - \rho v_i \frac{\partial \tilde{v}_j}{\partial x_j}. \quad (3)$$

By the weakly compressible approximation the divergence of the advection velocity  $\tilde{\mathbf{v}}$  is approximately zero and thus can be neglected. Hence, the final form of the momentum equation for a Lagrangian particle moving with  $\tilde{\mathbf{v}}$  is

$$\frac{\tilde{d}(\rho \mathbf{v})}{dt} = -\nabla p + \eta \nabla^2 \mathbf{v} + \rho \mathbf{g} + \nabla \cdot (\rho \mathbf{v} (\tilde{\mathbf{v}} - \mathbf{v})). \quad (4)$$

The last term on the right-hand-side is a consequence of the modified advection velocity and can be interpreted as the convection of momentum with the relative velocity  $(\tilde{\mathbf{v}} - \mathbf{v})$ . In the following we use the tensor  $\mathbf{A} = \rho \mathbf{v} (\tilde{\mathbf{v}} - \mathbf{v})$  for this term. Note the relation to the concept of Lagrangian mean motion [17].

### 2.1. Density summation

The density of each particle is calculated from a summation over all neighboring particles  $j$

$$\rho_i = m_i \sum_j W_{ij}, \quad (5)$$

where  $\rho_i$  and  $m_i$  denote the density and mass of particle  $i$ . As kernel function  $W_{ij} = W(\mathbf{r}_i - \mathbf{r}_j, h)$  we use the quintic spline function [18] with the smoothing length  $h$  set equal to the initial particle distance  $\Delta x$ . Note that the use of the density summation allows for density discontinuities, and, as the particle mass  $m_i$  does not change during a simulation, total mass is conserved exactly.

### 2.2. Conservation of momentum

The conservation equation for the momentum (4) is discretized following the standard SPH methodology in conservative form, i.e. using symmetric inter-particle pair forces. The properties  $\mathbf{v}$ ,  $p$ ,  $v$ ,  $\mathbf{g}$  and  $t$  in Eq. (4) are the particle velocity, pressure, kinematic viscosity, external body force and time, respectively. Using the inter-particle-averaged shear viscosity ( $\eta = \rho v$ )

$$\tilde{\eta}_{ij} = \frac{2\eta_i \eta_j}{\eta_i + \eta_j}, \quad (6)$$

together with the density-weighted pressure,

$$\tilde{p}_{ij} = \frac{\rho_j p_i + \rho_i p_j}{\rho_i + \rho_j} \quad (7)$$

the discretized momentum equation allowing for multi-phase problems is given by [8,19]

$$\frac{\tilde{d}\mathbf{v}_i}{dt} = \frac{1}{m_i} \sum_j \left( V_i^2 + V_j^2 \right) \left[ -\tilde{p}_{ij} \frac{\partial W}{\partial r_{ij}} \mathbf{e}_{ij} + \frac{1}{2} (\mathbf{A}_i + \mathbf{A}_j) \cdot \frac{\partial W}{\partial r_{ij}} \mathbf{e}_{ij} + \tilde{\eta}_{ij} \frac{\mathbf{v}_{ij}}{r_{ij}} \frac{\partial W}{\partial r_{ij}} \right] + \mathbf{g}_i. \quad (8)$$

Here,  $\mathbf{v}_{ij} = \mathbf{v}_i - \mathbf{v}_j$  is the relative velocity of particle  $i$  and  $j$ ,  $r_{ij}$  is the distance  $|\mathbf{r}_i - \mathbf{r}_j|$  between two interacting particles and  $\frac{\partial W}{\partial r_{ij}} \mathbf{e}_{ij}$  is the kernel-function gradient  $\nabla W(\mathbf{r}_i - \mathbf{r}_j, h)$ . The additional term on the right-hand-side approximates the divergence of the tensor  $\mathbf{A}$  using simply the average of both interacting particles  $i$  and  $j$ . Generally, the momentum equation can be discretized with SPH in various forms but we favor the above realization since due to the anti-symmetry the linear momentum is conserved exactly.

In the classical weakly-compressible SPH method the pressure of a fluid particle is obtained from the density by an equation of state in the form

$$p = p_0 \left[ \left( \frac{\rho}{\rho_0} \right)^\gamma - 1 \right] + \chi, \quad (9)$$

where  $p_0$ ,  $\rho_0$  and  $\chi$  are the reference pressure, reference density and background pressure, respectively. Following Morris et al. [18] the reference pressure  $p_0 = \gamma c^2 / \rho_0$  is calculated with an artificial speed of sound  $c$  and the exponent  $\gamma = 7$  to limit the density variation to 1%. Usually, the speed of sound is chosen at least one order of magnitude larger than the reference velocity to limit the effect of compressibility on the flow. With our new scheme we suggest to use  $\gamma = 1$  and  $\chi = 0$ , i.e.

$$p = c^2(\rho - \rho_0) = p_0 \left( \frac{\rho}{\rho_0} - 1 \right), \quad (10)$$

which reduces significantly the magnitude of spurious pressure.

### 2.3. Particle advection velocity

The key element in our proposed method is the modification of the particle advection velocity. Different from moving the particles with the momentum velocity we define a transport or advection velocity  $\tilde{\mathbf{v}}$  that is used to evolve the position of particles from one time step to the next by

$$\frac{d\mathbf{r}_i}{dt} = \tilde{\mathbf{v}}_i. \quad (11)$$

Using a constant background pressure field  $p_b$ , the particle motion takes advantage of the regularization and anti-clumping effect when advecting with the transport velocity  $\tilde{\mathbf{v}}$ . In particle notation, this velocity is obtained at every time-step  $\delta t$  from

$$\tilde{\mathbf{v}}_i(t + \delta t) = \mathbf{v}_i(t) + \delta t \left( \frac{\tilde{d}\mathbf{v}_i}{dt} - \frac{1}{\rho_i} \nabla p_b \right), \quad (12)$$

Note that although  $\nabla p_b = 0$ , the SPH discretization of  $\nabla p_b$  following Eq. 13 below is not 0th-order consistent and therefore generates a non-vanishing contribution. By simply calculating this discrete gradient of a constant pressure field  $p_b$  we incorporate the effect of the actual particle distribution to the motion of the fluid. The discretized form of Eq. (12) is obtained from the standard pressure term discretization using only the position information of the neighbors of particle  $i$ . Thus, the background pressure  $p_b$  defines the magnitude of this force and occurs as a prefactor in Eq. (13). Using this relation it is straightforward to model multi-phase problems allowing for different reference pressures in different phases. The resulting discrete pressure forces are non-vanishing and create a more uniform pressure distribution. Also, attractive forces between particles with negative pressures from the equation of state are counterbalanced, and tensile instability is suppressed. In the same time we avoid using a background pressure directly in the momentum equation that can lead to pressure-driven instabilities or freezing of particles under very high background pressure conditions [20]. Another important aspect is that the shifting velocity is not decoupled from the momentum velocity since we only modify the momentum velocity by the discrete background-pressure gradient at each time-step. For a uniform particle distribution these contributions would cancel out so that in regions where the flow field is smooth and particles are uniformly distributed the two velocities are almost identical. But in regions with strong flow distortions where particles exhibit an inhomogeneous distribution the trajectory velocity is corrected by the background pressure effect and void regions are inhibited.

In discretized form the trajectory velocity of a particle  $i$  reads

$$\tilde{\mathbf{v}}_i(t + \delta t) = \mathbf{v}_i(t) + \delta t \left( \frac{\tilde{d}\mathbf{v}_i}{dt} - \frac{p_b}{m_i} \sum_j \left( V_i^2 + V_j^2 \right) \frac{\partial W}{\partial r_{ij}} \mathbf{e}_{ij} \right). \quad (13)$$

We use a background pressure  $p_b$  which is on the order of the reference pressure  $p_0$ . Generally, this pressure could be chosen arbitrarily large as long as the time-step criterion is adjusted properly as a large  $p_b$  can cause high accelerations. Note that

the additional force in Eq. (13) can be calculated simultaneously with the right-hand-side of the momentum equation so that the additional computational cost of this step is marginal.

#### 2.4. Time-integration scheme

To integrate the equation of motion and the momentum equation in time we adopt the so-called kick-drift-kick scheme as presented by Monaghan [3]. First, the intermediate momentum velocity and the shifting velocity are calculated for each particle using the pressure force  $\mathbf{f}_{(p)}$ , the viscous force  $\mathbf{f}_{(\eta)}$ , the body force  $\mathbf{g}$  and the background pressure force  $\mathbf{f}_{(p_b)}$

$$\mathbf{v}^{n+\frac{1}{2}} = \mathbf{v}^n + \frac{\delta t}{2m} (\mathbf{f}_{(p)}^{n-\frac{1}{2}} + \mathbf{f}_{(\eta)}^{n-\frac{1}{2}} + \mathbf{g}), \quad (14)$$

$$\tilde{\mathbf{v}}^{n+\frac{1}{2}} = \mathbf{v}^{n+\frac{1}{2}} + \frac{\delta t}{2m} \mathbf{f}_{(p_b)}^{n-\frac{1}{2}}. \quad (15)$$

This step is referred to as the kick step, as only velocities are updated. Using the advection velocity we shift the particles to their new positions by

$$\mathbf{r}^{n+1} = \mathbf{r}^n + \delta t \tilde{\mathbf{v}}^{n+\frac{1}{2}}. \quad (16)$$

Now, the density at the new time step  $n + 1$  is calculated from the updated positions using Eq. (5). At this stage the new inter-particle forces  $\mathbf{f}_{(p)}^{n+\frac{1}{2}}$ ,  $\mathbf{f}_{(\eta)}^{n+\frac{1}{2}}$  and  $\mathbf{f}_{(p_b)}^{n+\frac{1}{2}}$  are calculated with the intermediate momentum velocity and the new positions. Finally, the velocity at the full time-step is obtained from

$$\mathbf{v}^{n+1} = \mathbf{v}^{n+\frac{1}{2}} + \frac{\delta t}{2m} (\mathbf{f}_{(p)}^{n+\frac{1}{2}} + \mathbf{f}_{(\eta)}^{n+\frac{1}{2}} + \mathbf{g}). \quad (17)$$

Note, with this scheme the force calculation is performed only once per time-step since in the first sub-step the forces from the second sub-step of the previous time step are used.

For stability reasons the global time-step  $\delta t$  is taken as the minimum of the CFL-condition based on the artificial speed of sound  $c$  and the maximum flow speed  $U$

$$\delta t \leq 0.25 \frac{h}{c + |U|}, \quad (18)$$

the viscous condition

$$\delta t \leq 0.25 \frac{h^2}{\nu} \quad (19)$$

and the body-force condition

$$\delta t \leq 0.25 \sqrt{h/|\mathbf{g}|}. \quad (20)$$

#### 2.5. Boundary conditions

Symmetric and periodic boundary conditions are enforced by the use of mirror or ghost particles [21], respectively. These virtual points inherit the fluid properties from their corresponding real particle and are included in the force calculation to ensure full support of the kernel. Furthermore, in case of a symmetry condition the normal velocity component is flipped to mimic a symmetric velocity field. Solid walls are represented with real fixed particles where a Neumann-boundary condition for the pressure is imposed. The velocity at these particles  $\mathbf{v}_{solid}$  is interpolated from the adjacent fluid phase and adjusted to enforce the no-slip condition by

$$\mathbf{v}_{solid} = 2\mathbf{v}_{wall} - \mathbf{v}_{fluid}. \quad (21)$$

For details of this boundary treatment we refer the reader to our previous work [22].

### 3. Numerical examples

We use our proposed method to simulate a broad range of classical SPH test cases, including the challenging Taylor-Green vortex flow or the lid-driven cavity problem. We want to emphasize that the current formulation does not require any additional parameters that need to be adjusted for each problem. The same numerical setup is used for all cases. More precisely, in all examples the speed of sound is chosen ten times larger than the characteristic reference velocity of the problem, and as background pressure for the advective acceleration we use the reference pressure  $p_0$  from the equation of state.

### 3.1. Flow around a periodic lattice of cylinders

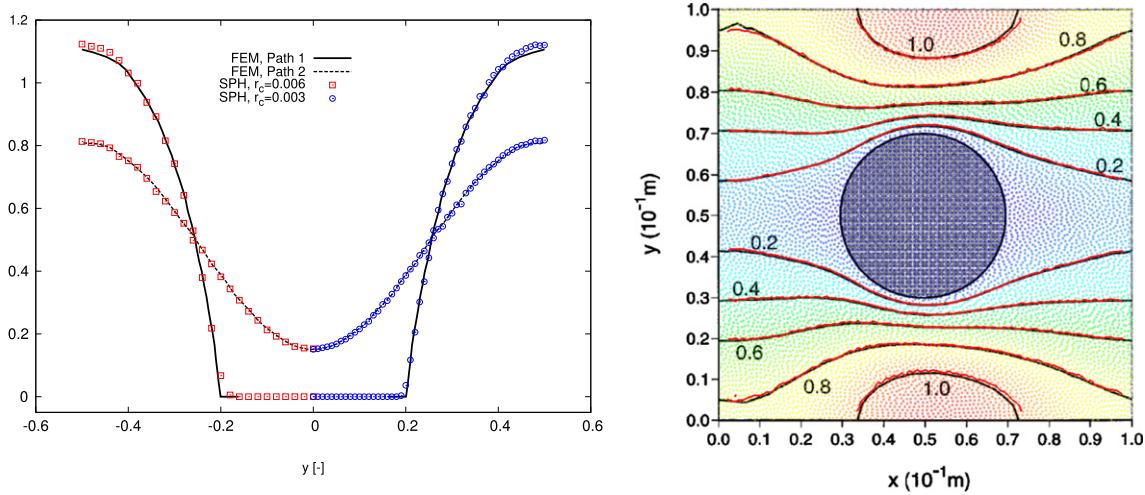
In the following example we study the flow through a periodic lattice of cylinders as presented in Morris et al. [18]. In this example all data are given in dimensional form as in the reference. A cylinder of radius  $R = 0.02$  m is placed in a square box with length  $L = 0.1$  m and the driving body force in  $x$ -direction is  $g = 1.5 \times 10^{-7}$  m/s<sup>2</sup>. The fluid is characterized by  $\rho = 1000$  kg/m<sup>3</sup> and  $\nu = 10^{-6}$  m<sup>2</sup>/s and taking the velocity scale to be  $U_{ref} = 5 \times 10^{-5}$  m/s gives a Reynolds number of one. We apply periodic boundary conditions at all boundaries to represent the periodic lattice of cylinders. If this case is simulated with the classical SPH method it is necessary to use a suitably adjusted constant background pressure in the equation of state to avoid void regions without particles in the wake behind the cylinder. The proposed method, however, works well without background pressure in the equation of state. The advective background pressure  $p_b$  is fixed as described above and does not require problem-specific adjustment.

The described geometry is discretized with Cartesian particles with an initial spacing of  $\Delta x = 0.002$  m and 0.001 m in both directions, thus a total of 2500 particles and 10,000 particles is used, respectively. We compare our results with the finite element method (FEM) reference results of this problem given in [18]. Fig. 1(a) shows two velocity profiles of the axial velocity component  $V_x(y)$  as function of the height of the periodic box for the two resolutions. The profiles are taken along vertical lines at  $x = L/2$  (Path 1) and  $x = L$  (Path 2), i.e. through the center of the box and at the exit of the domain. We find very good agreement in the presented velocity profiles indicating that we obtained converged results. The discrepancy of the velocity profile close to the cylinder surface is caused by the smoothing of the results due to interpolating the particle data onto the vertical lines. With increasing resolution this interpolation error vanishes, see the results at the higher resolution.

Morris et al. [18] also present contour plots of the velocity magnitude in the periodic box. In Fig. 1(b) we superpose their FEM reference results with the flow field extracted from our high-resolution simulation (red lines) using the same velocity scale ( $V_{ref} = 10^{-4}$  m/s) for non-dimensionalization and find excellent agreement.

### 3.2. Channel flow through periodic array of cylinders

To further validate our method we analyze the drag on a cylinder in a periodic channel. The drag is an integrated quantity over the cylindrical surface and is therefore a suitable parameter to quantify the accuracy of a numerical simulation. Different from the previous example, the flow is now wall-bounded at the upper and lower boundaries with a channel height of  $H = 4R$ , where  $R = 0.02$  m is the radius of the cylinder. The cylinder is placed on the centerline of the channel and the total length of the periodic channel segment is  $L = 0.12$  m, thus the inter-cylinder distance is  $6R$ . The liquid has a density and viscosity of  $\rho = 1000$  kg/m<sup>3</sup> and  $\eta = 0.1$  kg/(ms), respectively. A very detailed study of this problem using standard weakly-compressible SPH is presented in Ellero and Adams [23]. Different to their approach, here we do not adjust the body force in time to achieve a specified, constant mass flux but use a constant driving force  $g = 2.5 \times 10^{-4}$  m/s<sup>2</sup> in  $x$ -direction that yields an average flow velocity of similar magnitude as their imposed flow ( $\langle v \rangle = 1.2 \times 10^{-4}$  m/s). Note that, as we are com-



(a) Velocity profiles  $V_x(y)$  at  $x = L/2$  (Path 1) and  $x = L$  (Path 2) (b) Contour plots of velocity magnitude scaled with  $10^{-4}$  m/s.

**Fig. 1.** Comparison of SPH results with FEM reference results [18] for the flow through a periodic lattice of cylinders at  $Re = 1$ , references reproduced with permission of Elsevier.

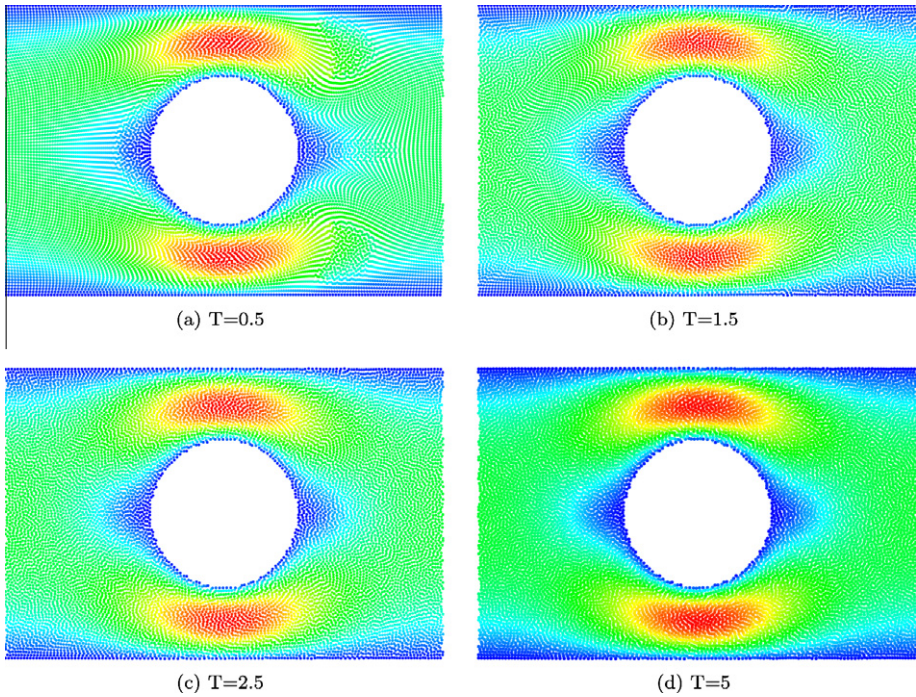


**Fig. 2.** Snapshots of the particles at various time steps colored with the magnitude of the velocity in the range between 0 (blue) and  $3\langle v \rangle$  (red) using 96 particles spanning the channel height.

paring non-dimensional results, the exact flow rate is not important as long as the flow characteristics are similar (the Reynolds number in our simulation differs only by about three percent from  $Re = 2.4 \times 10^{-2}$  given by Ellero and Adams [23]). For this example the dominating criterion for determining the speed of sound is the body-force scale and we use  $c = 0.1\sqrt{|\mathbf{g}R|} = 2.236 \times 10^{-4}$  m/s. As shown before, with the proposed method the region behind the cylinder is filled with particles immediately after starting the flow, unlike standard SPH that requires a specifically adjusted background pressure in the equation of state to avoid void regions.

As example, Fig. 2 shows several snapshots of the flow using 96 particles spanning the channel height, i.e. a total of 13,824 particles is used in this case. The particles are colored with the magnitude of the local velocity where the colormap ranges from 0 (blue)<sup>1</sup> to  $3\langle v \rangle$  (red). The time is scaled with the reference time  $t_0 = R/\langle v \rangle$  to indicate the initial transient phase in terms of the characteristic time of the flow.

As we start the simulation from a lattice configuration, i.e. particles are initialized on nodes of a regular Cartesian lattice, it takes several characteristic times to obtain a homogenous particle distribution. After  $T = 2.5$  the particle distribution is fully homogeneous. Steady-state quantities are extracted thereafter. The drag coefficient is defined as

$$C_D = \frac{F_D}{\eta\langle v \rangle}, \quad (22)$$

where  $F_D$  is the drag force exerted on the cylinder by the fluid. Note that due to symmetry in  $y$ -direction with respect to the center of the cylinder the only unbalanced force on the cylinder is  $F_D$  in  $x$ -direction. Instead of integrating the total stress along the cylinder surface, with particle methods it is straightforward to add all the force interactions between fluid and cylinder-wall particles in order to calculate the resulting drag on the cylinder [23].

Fig. 3 shows the temporal evolution of the drag coefficient obtained from SPH simulations using three resolutions with  $\Delta x = H/48$ ,  $\Delta x = h/96$  and  $\Delta x = H/192$ . The black dashed line denotes the reference result of Liu et al. [24], who obtained a drag coefficient of 106.76 for this case using a FEM code.

At early times, the extracted drag coefficient shows strong variations due to the rearrangement of particles from the initial lattice configuration, as can be seen from the particle snapshots. Later, only small fluctuations around the steady-state can be observed, and with increasing resolution the magnitude of these fluctuations decreases. The agreement with the reference value is very good and with increasing resolution we observe convergence to the exact value.

<sup>1</sup> For interpretation of color in Figs. 1–3, 5, and 7–13 the reader is referred to the web version of this article.

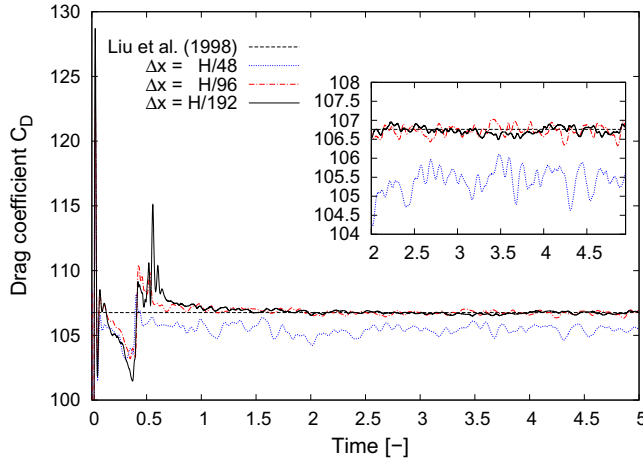


**Fig. 3.** Drag coefficient evolution: comparison of SPH results at three resolutions and the steady-state results of Liu et al. [24].

### 3.3. Taylor–Green vortex at $Re = 100$

We simulate the two-dimensional Taylor–Green flow at  $Re = 100$  to show that our new approach does not suffer from particle clustering. The analytical solution of the incompressible Navier–Stokes equation for this periodic array of vortices is given by

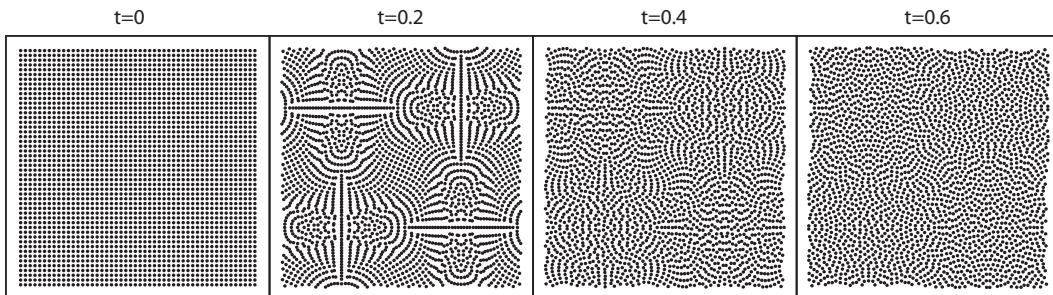
$$u(x, y, t) = -Ue^{bt} \cos(2\pi x) \sin(2\pi y) \quad (23)$$

$$v(x, y, t) = Ue^{bt} \sin(2\pi x) \cos(2\pi y). \quad (24)$$

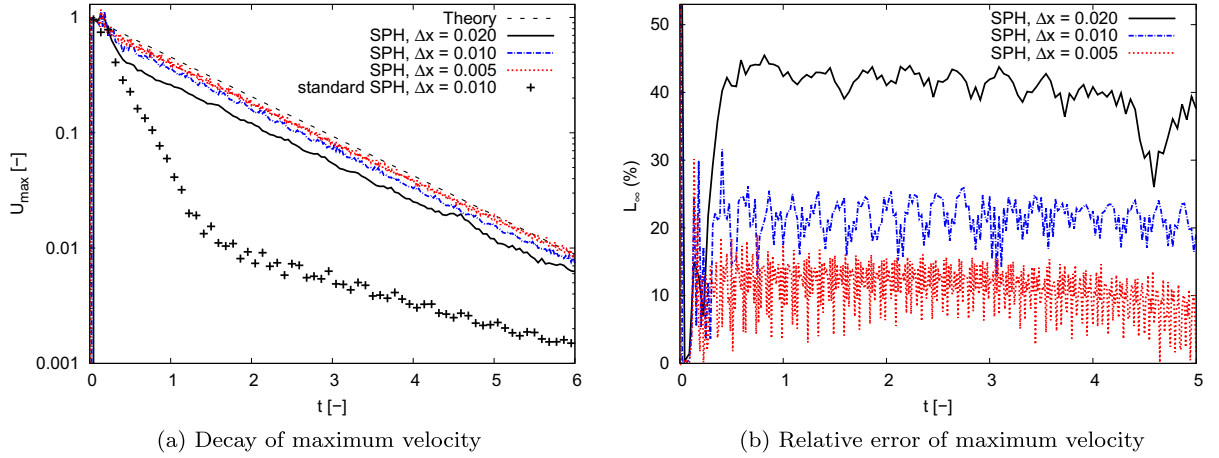
It is used as initial velocity distribution at  $t = 0$  and as reference solution to check the accuracy of our simulations. The decay rate of the velocity field  $b$  is  $-8\pi^2/Re$ , where  $Re = \rho UL/\eta$  is the Reynolds number obtained from the maximum initial velocity  $U$ , the density and viscosity of the fluid  $\rho$  and  $\eta$  and the length of the periodic vortex array  $L$ . In our simulations we use a domain with unit length  $L = 1$  and apply periodic boundary conditions in both coordinate directions. At  $t = 0$  we initialize the velocity of the particles with the analytical solution using a reference velocity of  $U = 1$ . We vary the initial particle spacing to study the influence of the resolution and use  $\Delta x = 0.02$  ( $50 \times 50$  particles),  $\Delta x = 0.01$  ( $100 \times 100$  particles) and  $\Delta x = 0.005$  ( $200 \times 200$  particles).

Fig. 4 shows several snapshots of the particle distribution for the Taylor–Green vortex at  $Re = 100$  using 2500 particles ( $50 \times 50$ ). At  $t = 0.2$  it is clearly visible that some particles are aligned with the stagnation lines of this flow. Standard SPH applied to this case starting from a regular lattice particle distribution results in a wrong decay of the vortex. Our current method does not suffer from such an error, produces a homogeneous particle distribution and predicts the correct decay rate.

A comparison of the decay of the maximum velocity is shown in Fig. 5, where the decay and error of the maximum velocity over time are shown. Using a log scale the analytical maximum velocity decays linearly with the slope  $-b$ . Our simulation results show the correct decay rate but with a small shift in the absolute magnitude of the vortex velocity, see Fig. 5(a). This difference is due to the rearrangement of the particles at early times ( $t < 0.5$ ) which causes the small peak and subsequent decrease of the maximum velocity. To show the improvement of our new scheme we also plot the result obtained from the standard weakly-compressible SPH approach, see the crosses in the figure. With the standard SPH method the maximum velocity decay is largely overpredicted and does not converge to the analytic solution (not shown here). The new proposed



**Fig. 4.** Particle snapshots for the Taylor–Green problem at  $Re = 100$  with a resolution of  $50 \times 50$  particles.



**Fig. 5.** Simulation results for the Taylor–Green problem at  $Re = 100$  with particles initially on a Cartesian lattice.

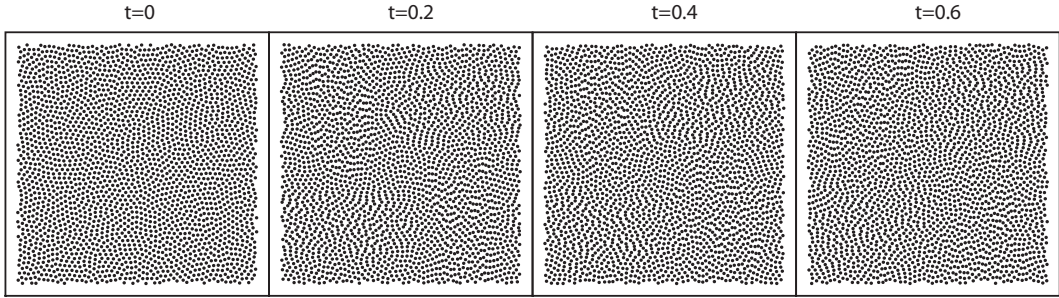


**Fig. 6.** Particle snapshots for the Taylor–Green problem at  $Re = 100$  using 2500 particles.

method shows satisfactory agreement with the analytical decay rate and we find first-order convergence in the relative error of the maximum velocity  $L_\infty(t)$ , see Fig. 5(b). The error norm  $L_\infty(t)$  is defined as

$$L_\infty(t) = \left| \frac{\max(|\mathbf{v}_i(t)|) - U e^{bt}}{U e^{bt}} \right|. \quad (25)$$

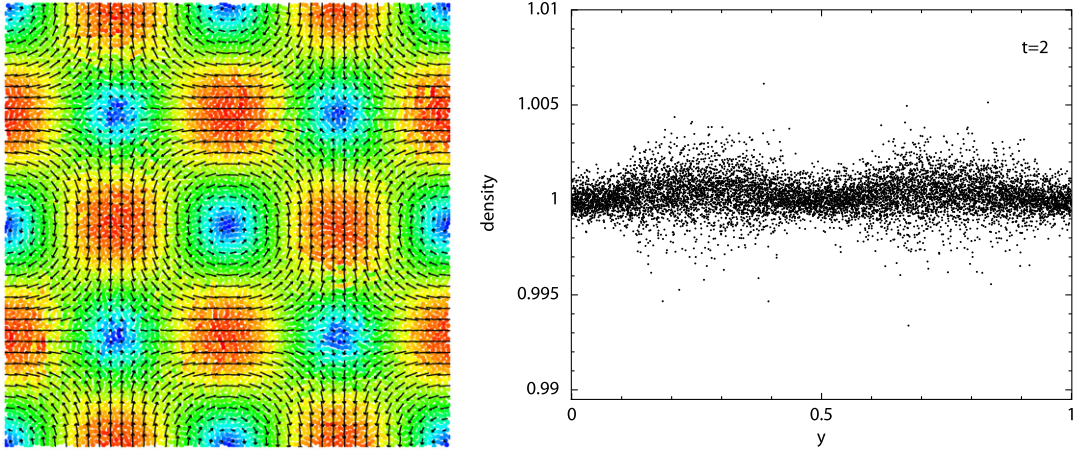


**Fig. 7.** Instantaneous velocity field and spatial density variation at  $t = 2$  for the Taylor–Green flow at  $Re = 100$ .

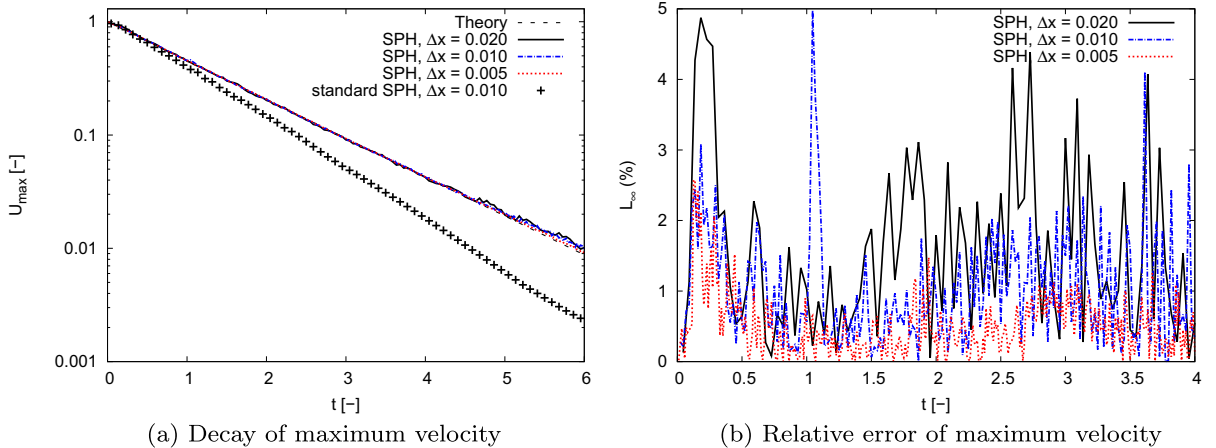


**Fig. 8.** Simulation results for the Taylor–Green problem at  $Re = 100$  using a relaxed initial particle distribution.

To avoid the particle rearrangement at the beginning which causes the shift in the maximum velocity, we use the final particle distribution of the previously presented results as initial condition and impose the analytical velocity profile at  $t = 0$ . Now, the particles are uniformly distributed during the entire simulation as shown in Fig. 6.

We also show the absolute velocity field with velocity vectors for this case at  $t = 2$  in Fig. 7(a). Here, the colormap ranges from 0 (blue) to  $U_{max}(t = 2)$  (red). Velocity vectors are scaled to clearly show the structure of the flow. At this point we want to highlight the smoothness of the velocity field and remember that we do not use any additional smoothing, reinitialization, or remeshing scheme in our method. Supporting this fact, Fig. 7(b) shows the density of all particles at  $t = 2$  simply plotted as function of the  $y$ -coordinate. The small scattering regions occur in the vicinity of the stagnation points, note however, that the total density variation is well below one percent.

The decay of the maximum velocity over time and the relative error for the Taylor–Green flow at  $Re = 100$  using a relaxed particle distribution at  $t = 0$  is shown in Fig. 8. The strong particle rearrangement as for the lattice setup case is avoided, and the initial overshoot in maximum velocity does not occur. The results for the three resolutions shown in Fig. 8(a) are almost identical and agree well with the analytical decay. Similarly to the previous case, from error plot we find approximately first-order convergence. The maximum error is remarkably reduced below five percent even for the lowest resolution of  $50 \times 50$  particles. We also show the decay rate obtained with standard SPH in Fig. 8(a). The result with the standard SPH also shows now a linear decay when starting from a relaxed particle configuration, but the decay rate is strongly overestimated.

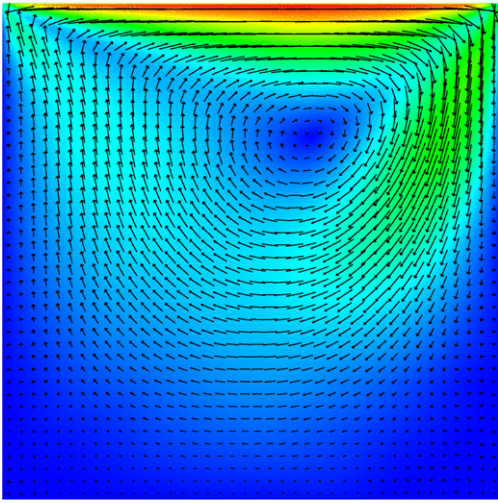
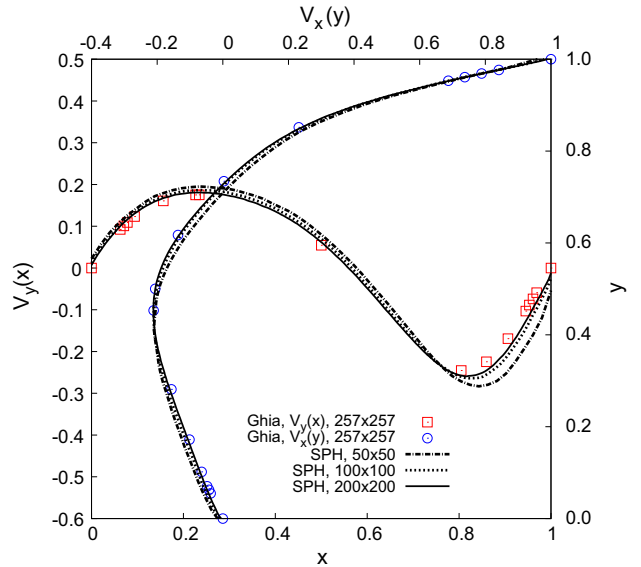
To the knowledge of the authors this is the first time that a weakly-compressible SPH method gives consistently correct results at different resolutions for the Taylor–Green vortex problem with a fully explicit scheme. Especially the accuracy of simulations starting from an initial Cartesian lattice particle configuration shows a strong improvement by the current approach. Note that for practical applications such an initial particle configuration is much more convenient than relaxed configurations that require pre-runs.

### 3.4. Lid-driven cavity

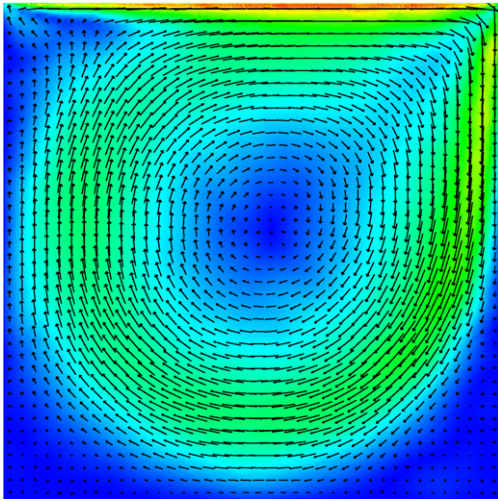
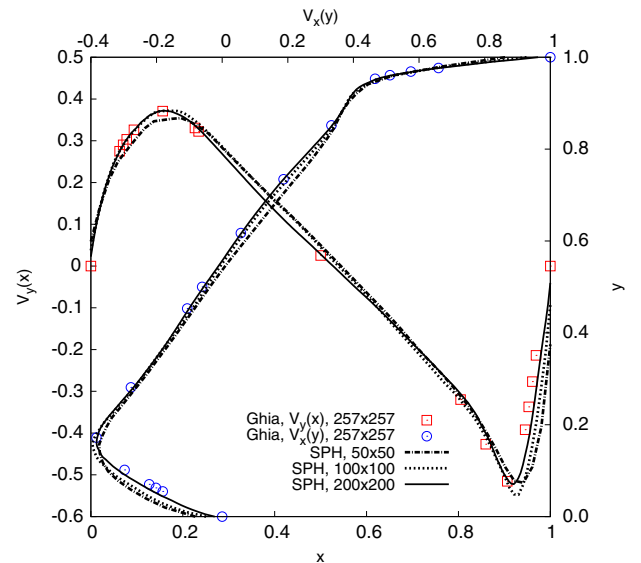
Another well-known and challenging test-case for SPH is the lid-driven cavity problem. A rectangular cavity with side length  $L = 1$  is filled with a fluid, and the top wall moves at a constant speed  $U_{max} = 1$ . We simulate the flow in the cavity for three Reynolds numbers  $Re = 100$ ,  $Re = 1000$  and  $Re = 10,000$  by adjusting the viscosity of the fluid accordingly, while fixing the density to  $\rho_0 = 1$ . The speed of sound for the equation of state is taken equal to  $c = 10U_{max}$ .

Two main difficulties arise in the lid-driven cavity problem. First, two singularities occur at the upper corners due to the moving lid on the horizontal wall boundary and the no-slip condition on the vertical walls. Second, strong velocity gradients are present in the flow at  $Re = 10,000$  and several secondary vortices occur. As there exists no analytical solution for this problem we use as a reference the results of Ghia et al. [25], who simulated this case with a highly-resolved multi-grid finite-difference scheme on a  $257 \times 257$  mesh. We simulate all three variations with  $50 \times 50$ ,  $100 \times 100$  and  $200 \times 200$  particles initially placed on a regular Cartesian lattice, to check for convergence of our results and compare them with the reference. Different from previous SPH results of this problem, we do not use a background pressure in the equation of state (compare de Leffe et al. [26]) nor do we need to impose a very high sound-speed (Lee et al. [27] use  $c = 100U_{max}$ ). We consider the results once the steady-state of the flow has been reached. We have checked for the steadiness by monitoring that the total kinetic energy in the system remains constant in time.

A visualization of the steady velocity field at  $Re = 100$  is shown in Fig. 9(a). The colormap shows the magnitude of the velocity ranging from zero (blue) to  $U_{max}$  (red), and the velocity vectors visualize the structure of the flow. Essentially, a single core vortex develops in the upper half of the cavity due to the shear force at the moving wall, and the fluid in the lower

(a) Velocity field with vectors ( $200 \times 200$  particles)

(b) Velocity profiles on the horizontal and vertical centerline.

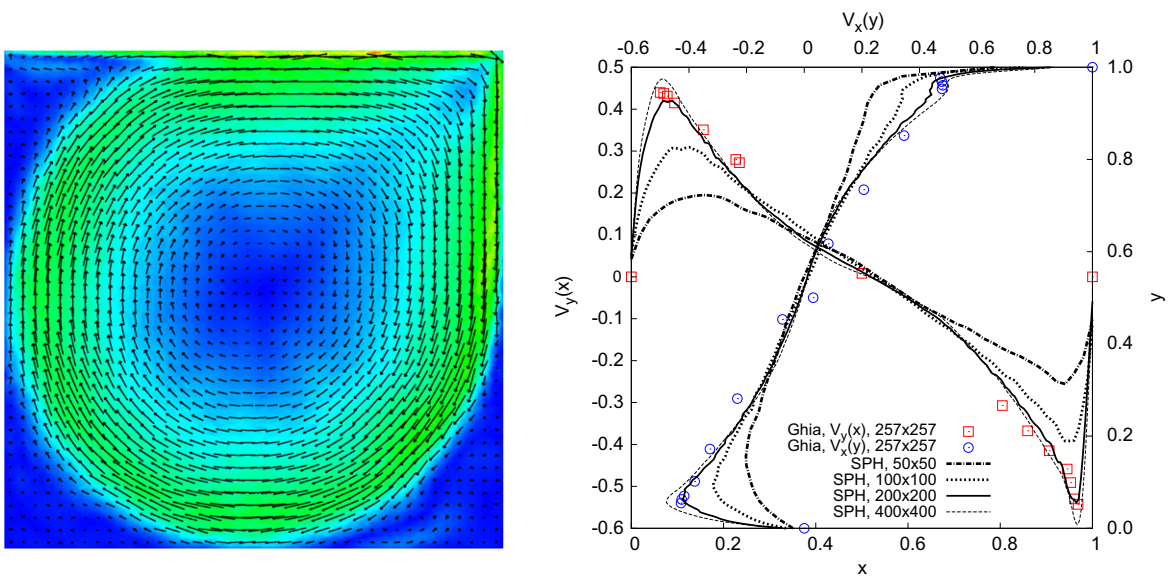
**Fig. 9.** Lid-driven cavity at  $Re = 100$ .(a) Velocity field with vectors ( $200 \times 200$  particles)

(b) Velocity profiles on the horizontal and vertical centerline.

**Fig. 10.** Lid-driven cavity at  $Re = 1000$ .

part of the cavity moves only slowly. A quantitative comparison with the reference is shown in Fig. 9(b), where the velocities in  $x$  and  $y$ -direction are plotted along the vertical and horizontal centerline, respectively. The reference results by Ghia et al. [25] are denoted by the colored symbols (◻ for the velocity in  $y$ -direction along the horizontal centerline  $V_y(x)$  and ◌ for the velocity in  $x$ -direction along the vertical center line  $V_x(y)$ ). The simulated profiles agree well with the reference results and the two higher resolutions show only marginal difference, thus converged results were obtained. For such a low Reynolds number already the lowest resolution using  $50 \times 50$  particles gives satisfactory results.

The following Figs. 10 and 11 show the corresponding analysis for  $Re = 1000$  and  $Re = 10,000$ . From the flow field we observe that the core vortex is more centered with increasing Reynolds number and the intensity of the vortex increases. Furthermore, in agreement with Ghia et al. [25] we find secondary vortices in the two lower and the upper left corner, but due to



(a) Velocity field with vectors (200× 200 particles)

(b) Velocity profiles on the horizontal and vertical centerline.

**Fig. 11.** Lid-driven cavity at  $Re = 10,000$ .

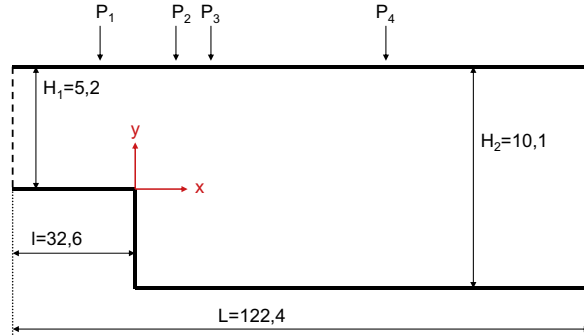
the scale of the velocity vectors they are hardly visible in the presented figures. At  $Re = 1000$  the velocity profiles along the centerlines match the reference results at all three resolutions. With higher resolutions we find a more accurate flow prediction in regions with strong velocity gradients (wall-near regions) but the core flow is approximated accurately even at the lowest resolution.

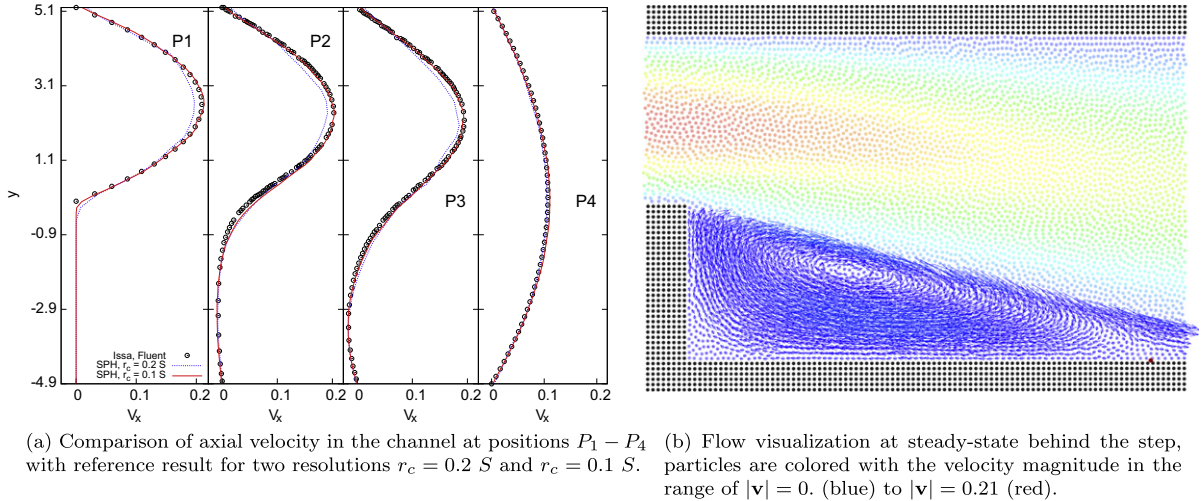
At  $Re = 10,000$  a much larger resolution is required to converge to the reference results, see Fig. 11. As mentioned earlier, the core vortex at this Reynolds number is almost centered in the cavity and secondary vortices develop. With the lower resolutions we underestimate the intensity of the center vortex. At the highest resolution presented here ( $200 \times 200$  particles) the agreement with the reference result is satisfactory, especially the modified velocity profile in the thin boundary layer at the upper wall is already captured nicely. Note that the reference results were obtained with a resolution of  $257 \times 257$  grid points.

The lid-driven cavity example demonstrates that our proposed method with the wall boundary formulation of our previous work [22] can be used to simulate accurately shear-driven flows with stagnation points at high Reynolds numbers.

### 3.5. Flow over a backward-facing step

Another wall-bounded flow driven by an external body force is the flow over a backward-facing step in a spanwise periodic channel. Fig. 12 shows a sketch and the dimensions of the geometry as presented in the work of Issa et al. [28]. The marked positions  $P_1$ – $P_4$  show the locations where we compare velocity profiles with the reference results. As there is no analytical solution for this example, the reference solution is obtained by a grid-based high-resolution simulation using FLUENT [28] (note, the resolution of the simulation using the Eulerian Finite-Volume method is not given in the reference).

**Fig. 12.** Sketch of the backward-facing step, lengths are given in mm.



(a) Comparison of axial velocity in the channel at positions  $P_1$ – $P_4$  with reference result for two resolutions  $r_c = 0.2\,S$  and  $r_c = 0.1\,S$ . (b) Flow visualization at steady-state behind the step, particles are colored with the velocity magnitude in the range of  $|v| = 0$ . (blue) to  $|v| = 0.21$  (red).

**Fig. 13.** Simulation results of the laminar flow over a backward-facing step.

The incompressible fluid is characterized by a density of  $\rho = 1$  and a kinematic viscosity of  $\nu = 1.456 \times 10^{-2}$ . Using twice the channel height above the step as hydraulic diameter  $D = 2h$  and a mean bulk velocity in the thinner channel above the step of  $U = 0.14$  gives a Reynolds number of  $Re = 100$ . The mean flow is driven by a constant body force in  $x$ -direction that was adjusted to achieve the specified mean bulk velocity. The speed of sound used for this simulation is ten times the maximum velocity in the channel above the step, i.e.  $c_s = 2.1$ .

Fig. 13(a) shows a comparison of the streamwise velocity over the channel height at four positions  $P_1$ – $P_4$  with the reference results from [28]. We plot the steady-state results of the flow field at two resolutions  $r_c = 0.2S$  and  $r_c = 0.1S$ , where  $S = 4.9$  is the step height. The instantaneous particle velocities were interpolated on a grid using the kernel  $W$  to obtain smooth profiles.

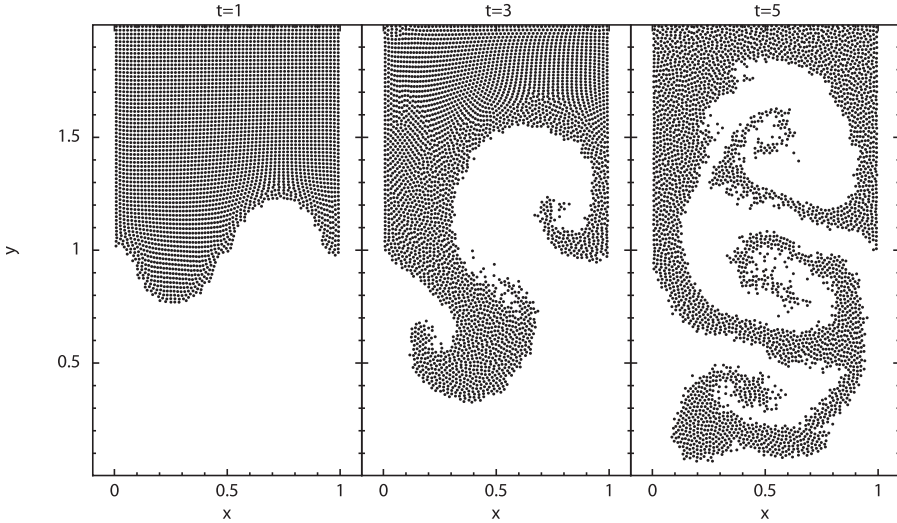
With the proper driving body force for the high resolution case to obtain the specified mean bulk flow at  $P_1$ , the agreement with the reference solution is very good. The results at  $P_2$  and  $P_3$  show that the recirculation bubble is well recovered, and far behind the step, the flow field again becomes parabolic, see  $P_4$ . Instead of fitting the driving force for each simulation we use the parameter from the highest-resolution case for all other simulations. Thus, the flow at  $r_c = 0.2S$  is slightly underpredicted but the overall agreement with the reference solution is still satisfactory. Also, this underprediction is reflected systematically in the consecutive profiles and shows that this effect could be scaled out by increasing the driving force.

Fig. 13(b) shows a snapshot of the simulation at steady-state in the vicinity of the backward-facing step. Particles are colored with the magnitude of the velocity in the range of  $|v| = 0$ . (blue) –  $|v| = 0.21$  (red) and only in the recirculation bubble we visualize the flow with velocity vectors. There are no void regions behind the step and the flow is well captured with the SPH method. The bold red dot in the figure denotes the reattachment point of the flow at the lower channel wall and is located at  $x_R = 6.2S$ . Issa [28] presents the reattachment point positions for the FLUENT and SPH results at  $x_R = 6.3S$  and  $x_R = 6.0S$ . Thus, our results agree well with the high-resolution grid data and the accuracy of the proposed SPH method is improved.

### 3.6. Rayleigh–Taylor Instability

We mainly applied our method to single fluid problems, but this last example shows that the modification of the particle advection velocity can also be used to simulate multi-phase problems. The Rayleigh–Taylor instability develops under the action of gravity when two fluids of different density are in contact and the heavier phase is on top of the lighter phase. We consider a rectangular domain of size  $L_x = 1$  and  $L_y = 2$  and use Cartesian particles to initialize the geometry. The density of the fluid in the lower part of the domain is set equal to one and above that phase the density is  $\rho_u = 1.8$ . To induce a well-defined instability the interface between the lighter and heavier phase is slightly disturbed following  $y > 1 - 0.15 \sin(2\pi x)$ . Gravity acts in negative  $y$ -direction and the Froude number is set to  $Fr = 1$ . The Reynolds number based on the reference velocity  $\nu_{ref} = \sqrt{L_y/2g}$  is  $Re = 420$  and defines the kinematic viscosity. Initially, all the particle velocities are zero and we use a resolution of  $60 \times 120$  particle for the fluids. The wall boundaries are modeled with non-moving SPH particles to enforce the no-slip boundary condition [22].

Fig. 14 shows the particles of the heavy phase for the Rayleigh–Taylor instability at three time instants  $t = 1, 3$  and  $5$ . Starting from the initial perturbation of the interface, initially two big plumes develop and the heavier and lighter phase are accelerated in opposite directions. Due to the relative motion shear forces act on the interface and produce interface roll-up.



**Fig. 14.** Snapshots of the heavy-phase particles for the Rayleigh–Taylor instability using  $60 \times 120$  particles at  $t = 1, 3$  and  $5$ .

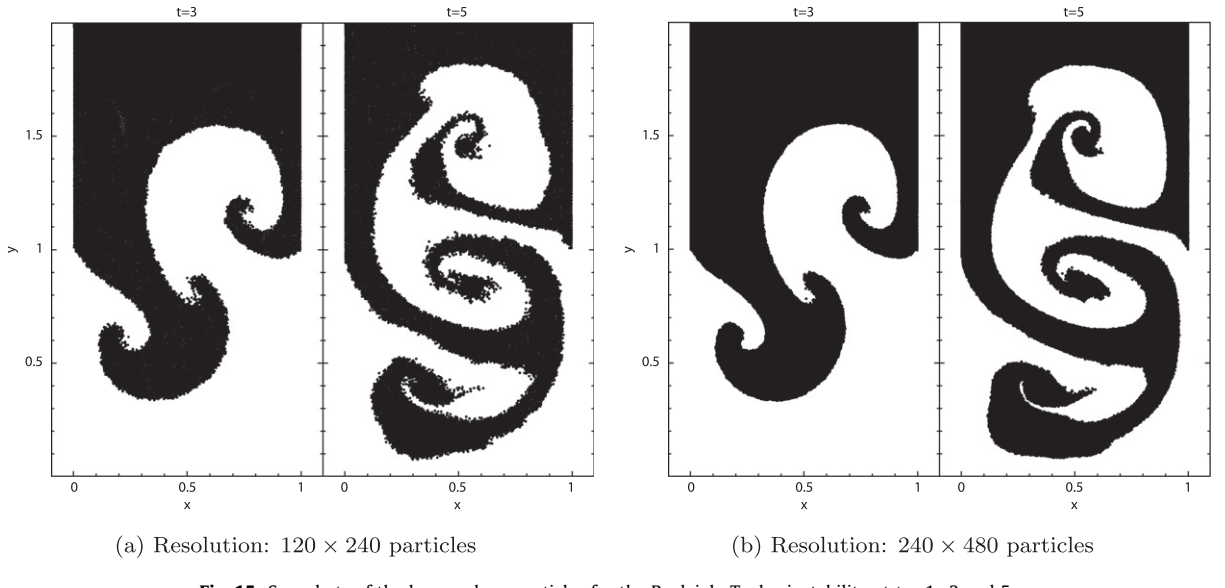


**Fig. 15.** Snapshots of the heavy-phase particles for the Rayleigh–Taylor instability at  $t = 1, 3$  and  $5$ .

**Fig. 15** shows the simulation results at  $t = 3$  and  $t = 5$  for two higher resolutions, each increased by a factor of two in both coordinate directions. Comparing all three cases we find that the main roll-up is well-captured at all resolutions and the shape of the main plumes at  $t = 3$  is converged. At later times, we observe similar secondary plumes as presented in Hu and Adams [4], who used an incompressible SPH method to simulate this case.

Finally, we present a high-resolution simulation of a three-dimensional Rayleigh–Taylor instability in a periodic box of size  $1 \times 1 \times 2$  using  $120 \times 120 \times 240$  particles, i.e. a total of about  $3.5 \times 10^6$  particles was used. The initial interface perturbation is now  $y < 1 - 0.15 \sin(4\pi x) \sin(4\pi y)$  and gravity acts in negative  $z$ -direction. **Fig. 16** shows the evolution of the volume-rendered lighter phase at  $t = 0, 2, 4$  and  $6$ . Note that here we only visualize 1.5 wavelengths but the domain covered two wavelengths of the disturbance. The initial interface disturbances grow with time and the plumes rise to the top of the container. Due to shear-forces the interfaces roll up and produce the well-known three-dimensional mushroom-shape structures. In the last frame of **Fig. 16** the lighter phase reaches the upper wall and the remaining liquid pushes upwards through the liquid bridges that have developed.

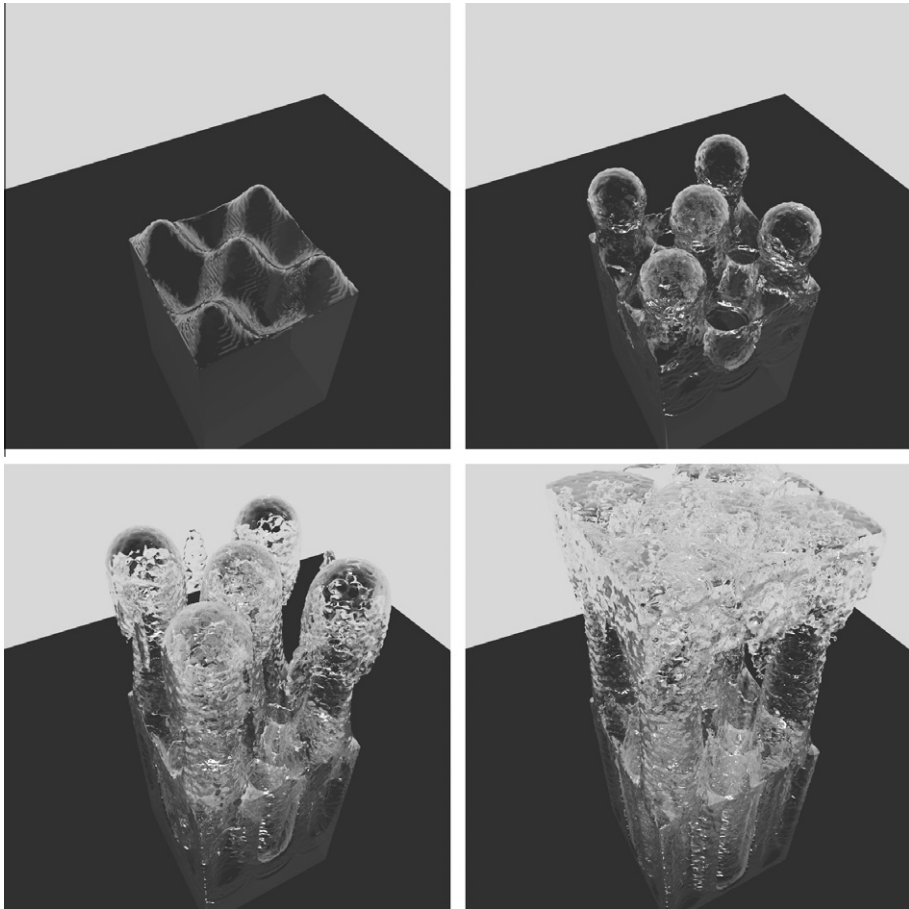


**Fig. 16.** 3D Rayleigh–Taylor instability.

#### 4. Conclusions

We have presented a simple modification of the advection scheme for SPH particles that allowed us to simulate many challenging problems that so far have suffered from the well-known tensile instability or the creation of void regions in the flow when computed by standard SPH. Due to the modification of the advection velocity an additional term appears in the momentum equation that is added to the standard method without any difficulties. This extra term and the modified advection velocity are the only necessary changes of the standard weakly-compressible SPH method as presented by Monaghan [3], without additional smoothing schemes or artificial viscosities. In all our problems we were able to use exactly the same setup, thus no empirical parameter has to be adjusted with this method. The main advantage of this method is its generality and simplicity while achieving unprecedented accuracy and stability properties even for flows at large Reynolds numbers. Extensions of this method to two-phase flows and free-surface flows are subject of ongoing research.

#### Acknowledgments

The authors gratefully acknowledge the postprocessing-tool *splash* from Daniel J. Price [29] which was used to produce some of the figures presented in this article. Furthermore we want to thank J. Biddiscombe [30] for the *pv-meshless*-plugins of Paraview that were also used for visualization purposes. Computational resources have been provided by the Leibniz Supercomputing Center (LRZ, High Performance Computing in Bavaria) under Grant *pr32ma*. Finally, we acknowledge the work of Sbalzarini et al. [31] who provided the Parallel Particle Mesh (PPM) Library that we used to implement our model and enables us to perform large-scale simulations on parallel computer architectures.

#### References

- [1] L.B. Lucy, A numerical approach to the testing of the fission hypothesis, *The Astronomical Journal* 82 (12) (1977) 1013–1024.
- [2] R. Gingold, J. Monaghan, Smoothed particle hydrodynamics – Theory and application to non-spherical stars, *Monthly Notices of the Royal Astronomical Society* 181 (1977) 375.

- [3] J.J. Monaghan, Smoothed particle hydrodynamics, *Reports on Progress in Physics* 68 (8) (2005) 1703–1759.
- [4] X. Hu, N. Adams, A constant-density approach for incompressible multi-phase SPH, *Journal of Computational Physics* 228 (6) (2009) 2082–2091.
- [5] S.J. Cummins, M. Rudman, An SPH projection method, *Journal of Computational Physics* 152 (2) (1999) 584–607.
- [6] R. Xu, P. Stansby, D. Laurence, Accuracy and stability in incompressible SPH (ISPH) based on the projection method and a new approach, *Journal of Computational Physics* 228 (18) (2009) 6703–6725.
- [7] A. Colagrossi, Numerical simulation of interfacial flows by smoothed particle hydrodynamics, *Journal of Computational Physics* 191 (2) (2003) 448–475.
- [8] X. Hu, N. Adams, A multi-phase SPH method for macroscopic and mesoscopic flows, *Journal of Computational Physics* 213 (2) (2006) 844–861.
- [9] S. Marrone, M. Antuono, A. Colagrossi, G. Colicchio, D. Le Touzé, G. Graziani,  $\delta$ -SPH model for simulating violent impact flows, *Computer Methods in Applied Mechanics and Engineering* 200 (13–16) (2011) 1526–1542.
- [10] A.M. Tartakovsky, P. Meakin, T.D. Scheibe, R. Eichlerwest, R.M.E. West, Simulations of reactive transport and precipitation with smoothed particle hydrodynamics, *Journal of Computational Physics* 222 (2) (2007) 654–672.
- [11] S. Adami, X. Hu, N. Adams, A conservative SPH method for surfactant dynamics, *Journal of Computational Physics* 229 (5) (2010) 1909–1926.
- [12] W. Dehnen, H. Aly, Improving convergence in smoothed particle hydrodynamics simulations without pairing instability, *Monthly Notices of the Royal Astronomical Society* 415 (June) (2012) 1–15.
- [13] D.J. Price, Smoothed particle hydrodynamics and magnetohydrodynamics, *Journal of Computational Physics* 231 (3) (2012) 759–794, <http://dx.doi.org/10.1016/j.jcp.2010.12.011>.
- [14] J. Monaghan, A turbulence model for smoothed particle hydrodynamics, *European Journal of Mechanics – B/Fluids* 30 (4) (2011) 360–370.
- [15] J.J. Monaghan, On the problem of penetration in particle methods, *Journal of Computational Physics* 82 (1) (1989) 1–15.
- [16] S. Lind, R. Xu, P. Stansby, B. Rogers, Incompressible smoothed particle hydrodynamics for free-surface flows: a generalised diffusion-based algorithm for stability and validations for impulsive flows and propagating waves, *Journal of Computational Physics* 231 (4) (2012) 1499–1523.
- [17] D.D. Holm, Fluctuation effects on 3D Lagrangian mean and Eulerian mean fluid motion, *Physica D: Nonlinear Phenomena* 133 (1–4) (1999) 215–269.
- [18] J.P. Morris, P.J. Fox, Y. Zhu, Modeling low Reynolds number incompressible flows using SPH, *Journal of Computational Physics* 136 (1) (1997) 214–226.
- [19] X. Hu, N.A. Adams, An incompressible multi-phase SPH method, *Journal of Computational Physics* 227 (1) (2007) 264–278.
- [20] O. Kum, W. Hoover, H. Posch, Viscous conducting flows with smooth-particle applied mechanics, *Physical Review E* 52 (5) (1995) 4899–4908.
- [21] P.W. Randles, L.D. Libersky, Smoothed particle hydrodynamics: some recent improvements and applications, *Computer Methods in Applied Mechanics and Engineering* 139 (14) (1996) 375–408.
- [22] S. Adami, X. Hu, N. Adams, A generalized wall boundary condition for smoothed particle hydrodynamics, *Journal of Computational Physics* 231 (2012) 7057–7075.
- [23] M. Ellero, N. Adams, SPH simulations of flow around a periodic array of cylinders confined in a channel, *International Journal for Numerical Methods in Engineering* 86 (8) (2011) 1027–1040.
- [24] A.W. Liu, D.E. Bonsire, R.C. Armstrong, R.A. Brown, Viscoelastic flow of polymer solutions around a periodic, linear array of cylinders: comparisons of predictions for microstructure and flow fields, *Journal of Non-Newtonian Fluid Mechanics* 77 (3) (1998) 153–190.
- [25] U. Ghia, K. Ghia, C. Shin, High-Re solutions for incompressible flow using the Navier–Stokes equations and a multigrid method, *Journal of Computational Physics* 48 (3) (1982) 387–411.
- [26] M. de Leffe, D. Le Touzé, B. Alessandrini, A modified no-slip condition in weakly-compressible SPH, in: T. Rung, C. Ulrich (Eds.), *Proceedings of the Sixth SPHERIC Workshop*, Hamburk, 2011, pp. 291–298.
- [27] E. Lee, C. Moulinec, R. Xu, D. Violeau, D. Laurence, P. Stansby, Comparisons of weakly compressible and truly incompressible algorithms for the SPH mesh free particle method, *Journal of Computational Physics* 227 (18) (2008) 8417–8436.
- [28] R. Issa, Numerical assessment of smoothed particle hydrodynamics gridless method for incompressible flows and its extension to turbulent flows, Ph.D. Thesis, University of Manchester, 2005.
- [29] D.J. Price, SPLASH: An Interactive Visualisation Tool for Smoothed Particle Hydrodynamics Simulations, *Publications of the Astronomical Society of Australia*, 2007. vol. 24, pp. 159–173.
- [30] J. Biddiscombe, D. Graham, P. Maruzewski, Visualization and analysis of SPH data, *ERCOFTAC Bulletin* 76 (2008) 9–12.
- [31] I.F. Sbalzarini, J.H. Walther, M. Bergdorf, S.E. Hieber, E.M. Kotsalis, P. Koumoutsakos, PPM A highly efficient parallel particlemesh library for the simulation of continuum systems, *Journal of Computational Physics* 215 (2) (2006) 566–588.